ASME Journal of Engineering for Gas Turbines and Power
Online journal at:
https://asmedigitalcollection.asme.org/gasturbinespower

Interaction Effects of Fan With Short Aero-Intake: A Multi-Objective Optimization Study With Modeling of Flow Coupling

Andrea Magrini[1]
Department of Industrial Engineering,
University of Padova,
via Venezia 1,
Padova 35131, Italy
e-mail: andrea.magrini@unipd.it

Ernesto Benini
Fellow ASME
Department of Industrial Engineering,
University of Padova,
via Venezia 1,
Padova 35131, Italy

The stronger coupling between the turbomachinery and the air inlet becomes more relevant in next-generation turbofan engines with low-pressure ratio fans and compact nacelles. This study presents a numerical investigation of the interaction between a transonic fan and a short aero-intake in terms of intake geometric design and fan modeling. The inlet design space is first explored in cruise and takeoff conditions, and the three-dimensional geometry is optimized in a multipoint and multi-objective formulation using a Bayesian solver to minimize the inlet distortion at takeoff and the total pressure losses in cruise. Flow coupling at high incidence is ensured through a body force model of the fan. The Pareto frontier highlights the conflicting nature of intake design between high incidence and high-speed performance. A selected individual from the Pareto is further examined by running unsteady full-annulus sliding-mesh simulations at a high angle of attack upon inlet separation. The detailed comparison of the flow field and the turbomachinery performance indicates an accurate reproduction of the inlet flow coupling through the body force model. Although lacking in fully replicating specific flow features near the tip of the blade, the simplified method allows reconstructing the blade response to inlet distortion and capturing the main flow structures. The study thus highlights the suitability of the adopted approach to simulate the mutual interaction between the fan and the inlet flow and provides an efficient method for the optimization of short-intake designs. [DOI: 10.1115/1.4070340]

Keywords: body force model, transonic fan, short intake, UHBPR, optimization

1 Introduction

The technological evolution of gas turbine engines for aircraft propulsion has seen a progressive enlargement of the engine size in civil applications due to the adoption of lower specific thrust propulsors with ultrahigh bypass ratios (UHBPR) [1]. To counteract the increase in fan diameter, the upcoming generation of medium to long-range aircraft engines will need to feature slimmer and more compact nacelle designs to reduce drag rise and limit installation losses [2]. On the intake side, this can be achieved by reducing its length L, relative to the diameter of the fan D, adopting shorter ducts with $L/D < 0.45$

In the last decade, numerous scholars have published research in the field of short aero-intakes for civil subsonic propulsion, investigating different aspects related to the specificity of the flow field arising and the differences with traditional longer ducts. In particular, three main effects appear to characterize short inlets:

- a reduced flow straightening capability, with residual velocity components at the fan face that bring enhanced swirl distortion even for attached flow and induce a non-uniform static pressure and mass flow;
- a stronger coupling with the fan that redistributes the mass flux and introduces a suction effect on the lip flow, retarding the flow separation that would develop in an equivalent unpowered situation;
- a conflict between drag and total pressure losses reduction due to slimmer and shorter profiles and fan efficiency degradation caused by higher distortion levels.

These phenomena have been widely described in the literature, mainly using computational fluid dynamics (CFD) simulations. Kennedy et al. [3] showed that the fan interaction can delay the intake stall even in a long duct with $L/D \approx 0.5$. Cao et al. [4] confirmed that the suppression of fan lip separation increases when L/D it is reduced from 0.44 to 0.17. Vadlamani et al. [5] detailed the mechanisms of the two-way interaction between a short inlet and the rotor at high incidence, evidencing a net spectral gap between the unsteadiness of the lip shock and the blade passing frequency. Mohankumar et al. [6,7] described the additional fan losses occurring in terms of excursion of the operating point caused by passage choking, blades ingesting a separated boundary layer, and loading redistribution due to radial flows. Gunn et al. [8] highlighted that the fan performance in short intakes is degraded at an increasing

---

[1] Corresponding author.

Manuscript received August 11, 2025; final manuscript received October 25, 2025; published online January 30, 2026. Assoc. Editor: Cis De Maesschalck.

angle of attack, even without flow separation, due to enhanced swirl distortion. Intake separation is driven by diffusion, rather than induced by shock waves, as in longer ducts. The shape of the lip has a clearly large impact on determining the status of the boundary layer and its interaction with the shock waves [9]. This coupling can be beneficial when fan suction promotes reattachment of the flow [10], but in short inlets, the unsteadiness associated with blade passing can destabilize the boundary layer, causing earlier separation in crosswind conditions [11]. This can be mitigated by reducing the diffusion upstream of the fan and the preshock Mach number [12].

The computational simulation of short intakes is expensive due to the need to model the fan interaction for physically representative results. Burlot et al. [13] compared different numerical fidelity methods for a low L/D geometry, finding that steady full-annulus Reynolds-Averaged Navier–Stokes (RANS) and actuator disk methods were unable to reproduce distortion transfer and only a body force model provided results closer to the averaged flow obtained with Unsteady RANS (URANS). Stuermer [14] restated the inability of the classic approach based on one-dimensional boundary conditions to simulate the flow past a short intake, using the DLR code TAU. A further comparison between this solver and the ONERA elsA code for fan/intake coupling is reported in Ref. [15].

In order to reduce the computational cost of expensive unsteady full-annulus simulations, alternative intermediate fidelity methods have been devised, collected under the name of body force models (BFM). These models simulate the cascade flow through volumetric source terms added to the RANS equations to replicate the work input of the blades without having to physically incorporate them using a body-fitted grid with a resolved boundary layer, thus offering substantial time savings [16]. Ma et al. [17] presented a mixed-fidelity approach based on their immersed boundary method with smeared geometry body force model that was shown to reproduce potential flow quantities and turbulence statistics in fan interaction with inlet distortion. Carnevale et al. [18] validated a BFM approach against a notional inlet, coming to the same conclusion. Several variants and improvements of BFM have been proposed over the years, and a complete review is outside the scope of this paper. These methods have been applied to study rotor-distortion interaction [19–21], fan-intake coupling [22–25], and boundary layer ingestion [26].

The available computational tools for intake modeling have been used in different design investigations. Peters et al. [27] presented one of the first design studies on varying L/D inlets combining URANS simulations with a developed BFM. The authors postulated an optimal L/D between 0.3 and 0.4, to balance the fan efficiency penalties with the possibility of reduced drag. Wang et al. [28] reported a surrogate-based optimization using differential evolution for a three-dimensional long-duct inlet parameterized via class-shape transformation to minimize the takeoff distortion at 28 deg of incidence.

Silva et al. [29] carried out a complete multipoint optimization of an ultrashort nacelle with an intake $L/D = 0.3$ considering takeoff, cruise, and crosswind operating points and modeling the fan with a modified parallel compressor model. Cao et al. [30] used an ensemble indicator of lip performance at multiple angles of attack and optimized its shape using a particle swarm algorithm operating on a Kriging surrogate model, but without fan modeling. Tao et al. [31] conducted a multipoint optimization with a multifidelity co-Kriging method to minimize drag in cruise and inlet pressure recovery at takeoff. The nacelle was parameterized with class-shape transformation on three aero-lines on the crown, keel, and sideline, but again no fan modeling was adopted. Monfaredi et al. [32] optimized the aeroacoustic performance on an axisymmetric intake by imposing the rotating static pressure field generated by the rotor on the fan face, computed in separate simulations. Yang et al. [33] used Kriging with differential evolution to minimize the takeoff distortion of an $L/D = 0.40$ inlet with steady full-annulus RANS simulations of the rotor. The postverification showed a DC(60) difference of +20% for the optimized intake simulated without fan modeling and −5% with URANS simulations of the rotor. In the latter case, the predicted efficiency was 1% lower than the steady RANS solution. Magrini and Benini [34] presented a parametric CFD investigation on the influence of lip shape parameters on the takeoff performance of a short inlet in the presence of fan interaction, finding relevant correlations between variables and showing a strong influence in neglecting the effect of the fan.

The literature review highlights the complexity of the interaction between short aero-intakes and the fan rotor at off-design conditions, which occurs on different time and spatial scales and involves both inviscid and viscous mechanisms. It is therefore mandatory to model such interaction when applying methods for short-inlet designs. Despite some authors making use of advanced algorithms in optimization studies, the lack of rotor modeling jeopardizes efforts to improve performance due to a nonphysical representation. The first part of this paper aims to extend the research on short inlet design by combining advanced optimization techniques with an established fan model, based on a body force method, to fully account for the mutual influence of the intake duct on the turbomachinery. The reduced shielding from the external flow and the enhanced interaction make the design of short inlets an inherent multi-objective task that is best addressed with specific optimization algorithms to identify the driving geometric parameters ensuring a sufficiently wide operating range. Starting from computational tools developed and validated in previous studies, this paper presents a series of investigations on a short intake of a UHBPR turbofan with $L/D = 0.35$ employing different fidelity methods, from BFM to full-annulus URANS simulations, culminating in a multipoint and multi-objective optimization using a state-of-the-art Bayesian solver. After that, the paper presents a detailed comparison of the adopted body force model of the rotor against reference full-annulus URANS simulations of a selected inlet geometry at takeoff, until separation. The second part of the study, therefore, provides a direct verification of the simplified modeling approach under distortion and assesses its ability to replicate the fan performance and the flow topology, validating the numerical approach used in inlet optimization.

The following Sec. 2 describes the parametric geometric model, the computational methods adopted, the performance metrics, and the optimization strategy. Section 3 reports the results of an initial design space exploration, used to find correlations between metrics and to set the optimization problem, followed by the analysis and discussion of the Pareto solutions obtained, eventually presenting the verification of the high-incidence flow past a sample intake using the BFM and higher accuracy URANS simulations.

2 Methods

2.1 Geometric Model. The geometry considered in this study is representative of a slim and compact nacelle for future UHBPR turbofans for a long-range passenger transport aircraft. The nacelle intake was represented through an in-house module building a fully parametric geometric model based on arbitrary curve types and a nonaxisymmetric shape. For the current problem, an inlet with a fixed $L/D = 0.35$ was modeled with cubic B-splines for the intake lip and diffuser, whose shape was controlled by the position of the respective control points. In particular, the lip aspect ratio AR and the throat contraction ratio $\mathrm{CR} = A_{\mathrm{hl}}/A_{\mathrm{th}}$ were directly specified, together with the scarf angle σ. The lip aspect ratio expresses the ratio between the axial and radial extension of the intake lip, from the highlight point (coincident with the leading edge of the fore cowl) to the throat. The contraction ratio measures the area ratio between the highlight and the throat section. The scarf angle measures the rotation of the highlight plane about the top dead center. The intake axis was drooped with respect to the engine axis by a fixed angle, due to the need to compensate the cruise upwash by aligning the inlet axis to the flow field.

The circumferential distribution of CR and AR was further controlled by cubic B-splines, explicitly setting the crown ($\theta = 0$ deg) and keel ($\theta = 180$ deg) values and allowing the

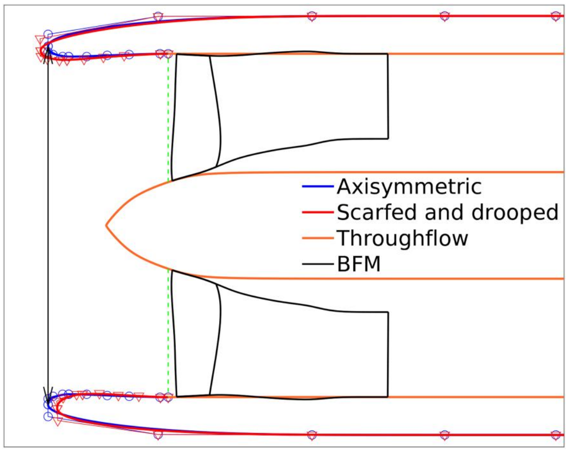

Fig. 1 Schematic of 3D nacelle parametric model with computational domain of fan rotor and throughflow geometry

intermediate azimuthal points to be smoothly connected, with the imposition of zero first and second derivatives at the top and bottom dead centers. A schematic of the parametric three-dimensional (3D) nacelle is shown in Fig. 1, where the blue curves represent an axisymmetric geometry in which the intake parameters (CR, AR) were first set. Droop and scarf, as well as azimuthal contouring, were applied through appropriate movements of the axisymmetric nacelle control points, resulting in the red curves and control polygons shown in the figure. The highlight plane, connecting the leading edges of the fore cowl, is marked with the arrow.

In addition to global size controls, local variations of the intake lip and diffuser curves were allowed, through relative displacements of the B-spline control points here denoted as ζ_i, setting the local curve shapes and the radius of curvature at the lip nose and throat. By adding to the six required local parameters ζ_i the two values of CR and AR at $\theta = 0$ deg and $\theta = 180$ deg, the scarf angle σ, and the highlight radius R_{hl}, a total of twelve design variables were employed. The variation of the highlight radius was set free in order to better accommodate the connection between the throat and the fan face. With the low L/D value chosen, in fact, the reduced axial extent cannot easily balance the need for a given contraction ratio, producing high diffusing angles. On the other hand, a change in the highlight area impacts the Mass Flow Capture Ratio MFCR $= A_\infty/A_{\mathrm{hl}} = \dot{m}/(\gamma p_\infty M_\infty^2 A_{\mathrm{hl}})$ in cruise, for a given engine thrust and flight conditions, changing the pre-entry drag component. For this reason, the allowed variation of the highlight radius, or equivalently of the ratio $2R_{\mathrm{hl}}/D$, was limited to give a corresponding cruise MFCR between 0.7 and 0.75.

A representation of the examined design space obtained by linear sampling of each design variable from the minimum value to the maximum value is shown in Fig. 2, where the highlight radius has been kept fixed for ease of understanding.

2.2 Numerical Models.

The numerical models adopted to simulate the intake geometries have been developed and validated in previous research [34] and are here briefly summarized. The reference geometry schematized in Fig. 1 was simulated using steady-state RANS CFD using the commercial solver Ansys Fluent [35]. The computational domain comprised the nacelle intake with the cylindrical outer cowl and a hemispherical far-field boundary. The internal duct varied according to the model adopted to reproduce the turbomachinery and the flight condition. The operating fluid was air, modeled as an ideal gas with a specific heat ratio $\gamma = 1.4$ and Sutherland's law for the viscosity. The turbulence closure was $k - \omega$ shear stress transport (SST) [36]. Second-order approximation was employed, with high-resolution schemes for convective fluxes and weighted least-squares gradient reconstruction. Freestream conditions were imposed on the Riemann farfield in terms of Mach number M, static pressure p and temperature T, and velocity vector orientation. The mass flowrate through the engine was controlled via the static pressure at the outlet of the duct. For the discretization of the computational model, a fully-structured multiblock grid with $y^+ < 1$ was automatically generated. The complete description of the model, including validation of grid spacing for NACA 1-series intakes and sensitivity to grid size, is thoroughly reported in Ref. [34]. An additional study on turbulence modeling is here reported in Fig. 3 for a sample geometry in terms of the Inlet Pressure Ratio (IPR, see Eq. (2)) and DC(60) (see Eq. (3)) versus the angle of attack α. Results provided by $k - \omega$ SST and Spalart–Allmaras are very similar and consistent.

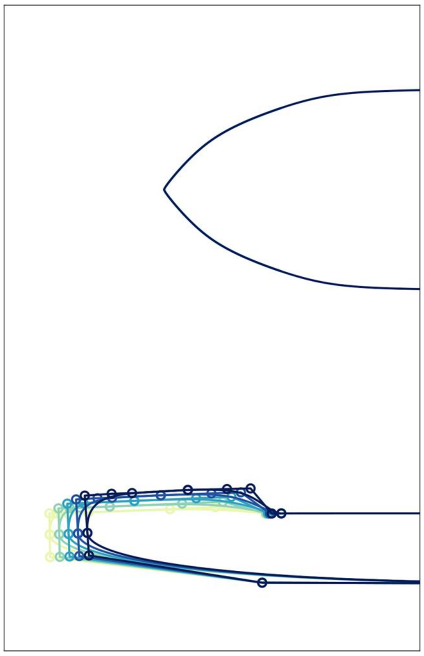

Fig. 2 Design space variation of parametric intake

The coupling between the engine and the inlet flow is mandatory for low L/D inlets with high incidence, as highlighted in the introduction. In this condition, two approaches were adopted. During the optimization, fan/inlet coupling was achieved by means of a body force model. As mentioned in Sec. 1, the BFM avoids the direct simulation of the turbomachinery blades by applying volumetric source terms in the Navier–Stokes equations to replicate the forces exchanged between the fluid and the cascade. The actual model derives from a development of the original L/D formulation of Thollet [37] and has the following equations:

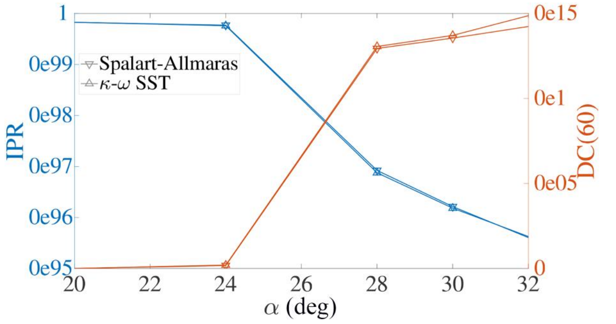

Fig. 3 Variation of inlet performance with the angle of attack for two turbulence models

$$
\begin{cases}
f_n = W^2 \dfrac{2\pi\chi}{h^*}\left(\beta - \beta_n^0\right) \\
f_p = \dfrac{K_p}{h^*} W^2 \\
K_p = K_p^0 + 2\pi\chi\left(\beta - \beta_p^0\right)^2
\end{cases}
\tag{1}
$$

f_n represents the streamline normal force, responsible for flow turning, and f_p the streamline parallel force, responsible for increase of entropy and losses. They are expressed using a semi-analytical formulation in terms of local flow variables (the relative velocity magnitude W and the relative velocity angle β), blade geometric parameters (row solidity χ and staggered pitch h^*), and local calibration coefficients ($\beta_n^0, \beta_p^0, K_p^0$). These coefficients are extracted from a unique 3D single-passage CFD simulation at the peak efficiency point, for a given rotational speed. Metal blockage is included to capture flow choking under transonic conditions. A detailed description of the model developed by these authors can be found in Ref. [38], where the actual implementation strategy modeling 3D blade features, the sensitivity to the force extraction method, the optimal calibration procedure and the numerical implementation are thoroughly reported. Compared to other body force models in the literature, this version relies on a semi-analytical expression of the forces requiring a single calibration for each speedline from CFD data, and it has been shown to provide physically consistent results for cases subject to inlet distortion. Although formulated for a circumferential-averaged flow, by providing local force values in each cell, the BFM is able to reproduce the flow field across a cascade with nonuniform inflow conditions, producing higher accuracy compared to full-annulus steady RANS solutions [13].

The validation of the computational model is presented here and briefly reported. The comparison between classic single-passage steady-state CFD solutions, the BFM results, and experimental data for the NASA GEAE R4 fan with outlet guide vanes (OGV) stage is reported in Fig. 4. The characteristic maps of Fig. 4(a) are well reproduced by both models, with the BFM giving a constant offset in the isentropic efficiency η_{iso}, but closely matching the curve shape. The spanwise distribution of the total pressure ratio (TPR) downstream of the OGV measured experimentally in two NASA wind tunnels [39,40] and computed numerically confirms the good agreement of both numerical methods with the experiment, with the BFM being able to reproduce the compression along the span.

The validated numerical setup for the NASA GEAE R4 stage was replicated to simulate a UHBPR fan stage designed to power the nacelle. The comparison between 3D CFD data and the body force solution of this fan stage is reported in Fig. 5, where the normalized $\widetilde{\text{TPR}}$ and $\widetilde{\eta_{\text{iso}}}$ maps are shown at full throttle and part speed. In both cases, the BFM appears to be sufficiently accurate to duplicate the CFD data and the machine behavior at varying mass flowrate, with a faithful reproduction of the efficiency curve, although with a slight underestimation of its level.

Throughout the optimization, the BFM model was adopted for the fan rotor only, in order to capture the coupling with the inlet flow at a lower computational cost. Thus, body forces were active in the volume swept by the blades, shown in black in Fig. 1. Downstream of the rotor, the static pressure outlet controlled the mass flowrate across the engine, running at constant rotational speed.

For BFM simulations, the full-annulus nacelle model was used, amounting to 6M cells. Instead, during cruise the interaction between the fan and the intake is much weaker, since the rotor operates with an almost purely clean flow, the incidence of the aircraft being low and the wing upwash and spanwise flow compensated by the nacelle installation angles. For this reason, in order to reduce the computational effort for the multipoint optimization described in Sec. 2.4, a half-model throughflow nacelle with a pressure outlet boundary condition was used for cruise simulations, employing the orange curves of Fig. 1. In this model, only half of the symmetric body is simulated, setting a symmetry boundary condition on the vertical plane. The impact of this approach will be examined in Sec. 3.3.1.

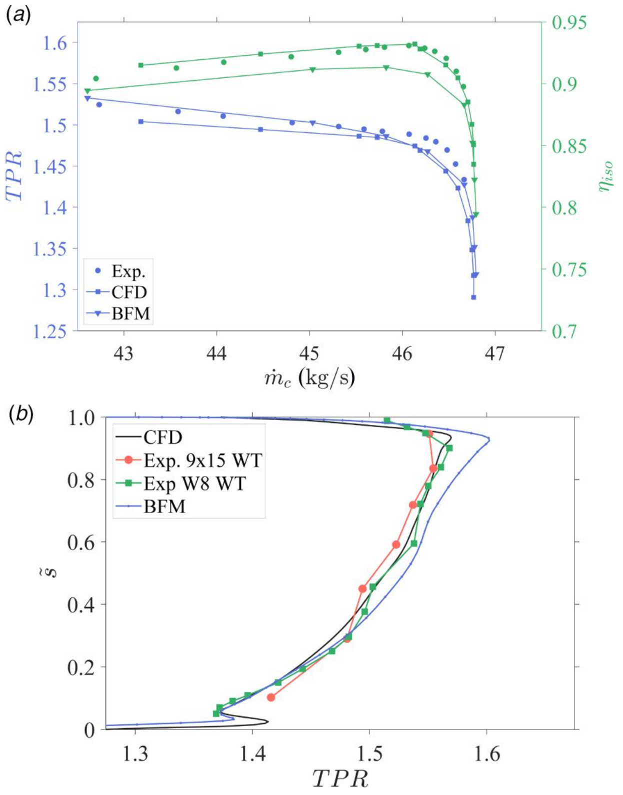

Fig. 4 Validation of R4 fan stage performance: (*a*) characteristic maps and (*b*) TPR spanwise distribution

In addition to BFM solutions, the UHBPR fan was simulated in the nacelle-installed configuration also by means of 3D CFD with an

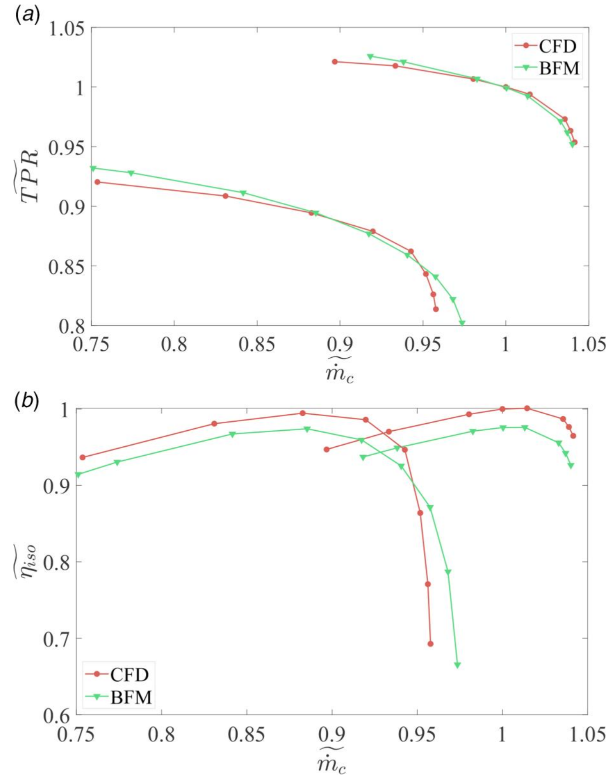

Fig. 5 Comparison of BFM and CFD models of UHBPR fan stage: (*a*) TPR characteristic and (*b*) isentropic efficiency characteristic

unsteady solution, to compare the intermediate-fidelity BFM result with a more accurate sliding-mesh full-annulus URANS simulation. The latter retained the validated approach for the NASA GEAE R4 in terms of mesh size and turbulence modeling. The total size of the grid, including the rotor blades, the external flow and the nacelle, was 60M. The time integrator was an implicit backward Euler method with second-order accuracy. The selection of the time-step was based on the indication of Stuermer [14], showing that for an analogous case, 1000 time steps per rotor revolution were large enough to capture the mean flow features and also show convergence of the unsteady loading amplitudes. The same value was used in Ref. [5]. For the current case, 990 time steps per rotor revolution were used, allowing to resolve up to 22 harmonics of the blade passing frequency. In addition, to reduce spurious reflections from the outlet and eliminate the effect of the outlet condition, a choked nozzle was used downstream of the fan. Note that the mesh of the BFM and the URANS simulations was identical, except for the block encapsulating the rotor, thus ensuring a consistent comparison between the two datasets.

2.3 Performance Metrics.

Intake performance was measured using different indicators. The boundary layer and shock losses are described by the Inlet Pressure Ratio, the ratio between the area-averaged aerodynamic interface plane (AIP) total pressure and the freestream value:

$$\mathrm{IPR} = \overline{p^0}_{\mathrm{AIP}}/p^0_\infty \qquad (2)$$

The AIP plane was placed just upstream of the rotor leading edge (dashed green line in Fig. 1).

Inlet distortion was quantified using the industry-standard DC(60) coefficient, measuring the difference between the minimum average total pressure in the most critical sector of amplitude θ and the AIP total pressure, divided by the AIP dynamic pressure:

$$\mathrm{DC}(\theta) = \frac{\overline{p^0}_{\mathrm{AIP}} - \overline{p^0}_{\min,\theta}}{\bar{q}_{\mathrm{AIP}}} \qquad (3)$$

For its calculation, an AIP rake grid was used, mimicking the experimental practice. Although SAE ARP1420 [41] prescribes different indicators, DC(60) remains an intuitive and widely used index. However, it is well known that it is unable to activate for certain distortion patterns, in particular in the presence of axisymmetric distortion or when it covers an area with a resolution smaller than the equal area sectors of the AIP total pressure rake used for its calculation [42]. For this reason, within the optimization process, where the genetic diversity between individuals can be low and a high resolution is needed, other distortion criteria appear to be more suitable. For this purpose, leveraging the denser resolution offered by CFD, the following index was defined, as employed in Ref. [34] and previously proposed in Ref. [8]:

$$\widetilde{D}_c(\phi) = \frac{1}{c}\sqrt{\iint (\phi - \phi_{\mathrm{ref}})^2 dc} \qquad (4)$$

where c can be the area (area-averaged) or mass flowrate (mass flow-averaged), ϕ denotes the distorted field, and ϕ_{ref} is the same field evaluated with clean inflow. For the rotor case, the clean inflow corresponds to the ducted rotor fed with a uniform flow at equal inlet-corrected mass flowrate. Once installed and exposed to intake coupling, the rotor operates with a varying distribution of flow parameters, among which the most susceptible to distortion is the total pressure. However, incidence effects also introduce a nonuniform mass flux, resulting in swirl angle nonomogeneity. Therefore, $\widetilde{D}_A(\beta)$ and $\widetilde{D}_{\dot m}(p^0)$ were selected as additional metrics, the former measuring the change in relative swirl angle β, that is, the incidence angle of the rotor ($\Delta\beta = \Delta i$), the latter being sensitive to the total pressure change across the entire fan face. Note that to maintain a nondimensional form, $\widetilde{D}_{\dot m}(p^0)$ was divided by the freestream total pressure.

When considering takeoff conditions, the engine thrust appears another important metric to consider, as it can drop due to inlet distortion, causing loss of flow compression or mass flux. To link the simulated rotor operation to thrust, an isentropic deswirl and expansion of the flow downstream of the rotor were supposed, giving the following expression of the isentropic axial thrust coefficient $C_{Fx,\mathrm{iso}}$:

$$C_{Fx,\mathrm{iso}} = \dot m \left[\sqrt{\left(\frac{2\gamma}{\gamma-1}RT^0\left(1-\frac{1}{\lambda}\right)^{\frac{\gamma-1}{\gamma}}\right)} - V_\infty\cos(\alpha)\right]\Big/(\dot m V_\infty) \qquad (5)$$

with $\dot m$ the mass flowrate, $\lambda = p^0/p_\infty$, V_∞ the flight speed, α the angle of attack, and all the stagnation parameters measured at the stage exit.

2.4 Optimization Strategy.

The computational framework described so far was used to perform a design space exploration and successive optimization of the inlet geometry that account for the fan coupling, considering two operating conditions. The first was the takeoff rotation, where the engine operates close to the maximum flow capacity and with a large highlight incidence, coming from the aircraft angle of attack and the upwash induced by the high-lift configuration of the vehicle with exposed slats and flaps. In this condition, the inlet must tolerate the high MFCR flow (>1.5) with no lip separation up to a sufficiently high incidence, to avoid dangerous thrust loss. The high flowrate means that the stagnation point of the ingested streamtube lies far from the highlight, on the external cowl, implying large flow turning and intense local acceleration past the lip, possibly causing shocks or diffusion-based separation and swirl distortion. It is well-known that the optimal intake features for low speed do not match well with the high-speed requirements of thin nacelles with small lip radii. For this reason, in addition to the takeoff condition the design study considered a second operating point in cruise. The difference in the flow field translates into the need for different objective functions in an optimization study.

The formalization of the optimization problem was performed after an initial design of experiment (DoE) that aimed to scan the design space to identify correlations between variables and performance metrics in the two operating conditions. After that, the following problem was solved:

$$\min \boldsymbol{F}(\boldsymbol{X}) = \begin{cases} f_1(\boldsymbol{X}) = 0.5DC(60) + 0.2\widetilde{D}_{\dot m}(p^0)\,@\,\mathrm{T/O} \\ f_2(\boldsymbol{X}) = 100(1-\mathrm{IPR})\,@\,\mathrm{cruise} \end{cases} \qquad (6)$$

The reason for the specific choice of the objectives will be given later, but it is apparent that at takeoff the distortion should be minimized, while in cruise the total pressure losses should be, the distortion being intrinsically low.

The boundary conditions for the first and second objectives are reported in Table 1.

The optimization algorithm used the state-of-the-art black-box optimization library BoTorch [43], which provides a modular and easily extensible interface for Bayesian optimization built on PyTorch, exploiting highly scalable and parallel implementations in multiple system architectures. The multi-objective optimization

Table 1 Operating conditions in the optimization

Op. point	Obj.	Alt. (m)	ISA (K)	Mach	AoA (deg)
Take-off (OP1)	f_1	0	15	0.26	24
Cruise (OP2)	f_2	10,600	0	0.85	4.85

problem was thus solved using a Bayesian solver in which the numerical observations were modeled as noiseless, using a constant basis function for the Gaussian process mean with a Matérn covariance.

The cost of direct function evaluation in the present problem is high. The optimization time could be reduced by evaluating multiple sampling points at the same time. However, maximizing the utility of the acquired information suggests limiting the number of concurrent evaluations to a small number. During the optimization, no parallel individual objective computation was adopted, but instead the parallelism was exploited inside the objective function call, i.e., for the multipoint simulations of each individual.

A task-based paradigm was implemented to run an arbitrary number of operating points for a list of individuals using a task scheduler. The workflow of the procedure is depicted in Fig. 6. Given a set of n individuals to be evaluated at m operating points, a q-task parallel pool was created. Each task was bound to a single individual x_k and submitted m simulations to a remote computing server job scheduler. The total number of concurrent simulations was thus $q \times m$. Each of the m simulations was assigned an amount of computational resources (i.e., number of processes for parallel CFD simulations) based on the computational weight of the operating point. Considering N the number of processes per individual, $N_i = w_i N$ parallel processes were allocated for the i operating point, $i = 1, \ldots, m$, with w_i the weight of the operating point. In total, $N \times q$ processes ran in parallel. Downstream of the job allocation in the computing server, a synchronization point ensured that the m operating points of the x_k individual had been completed, before filling the parallel pool with a new one. Since the weight was chosen to be proportional to the computational time, the conclusion of the m operating points was almost synchronous, maximizing the parallel efficiency.

In the optimization, $q = 1$ and $m = 2$, with $w_1 = 0.74$ and $w_2 = 0.26$ (1 refers to takeoff, 2 to cruise, see Table 1). The average computational time per individual was 130 CPUh for OP_1 and 46.5 CPUh for OP_2. During the initial DOE evaluation or when the list of individuals to be simulated was known in advance, $q > 1$. If the total available computational budget N_{tot} remains fixed, which is typically the case, assuming perfect parallel scaling and zero queue time, the number of individual simulations in a given amount of time remains fixed. In fact, the total computational time per individual is given by

$$t_k = \sum_{i=1}^{m} \frac{t^{(i)}}{\frac{N_{\mathrm{tot}}}{q} w_i} \tag{7}$$

where $t^{(i)}$ is the reference computational time for the operating point OP_i. Since

$$w_i = \frac{t^{(i)}}{\sum_{j=1}^{m} t^{(j)}} \tag{8}$$

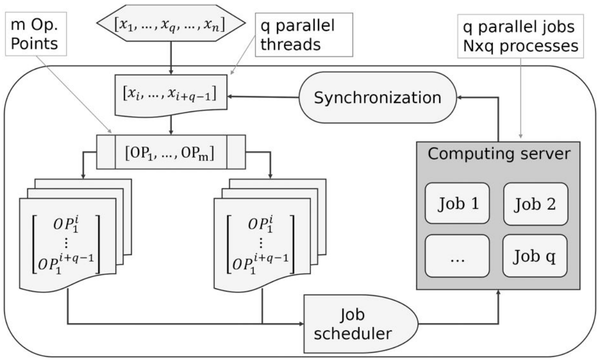

Fig. 6 Workflow of the parallel simulation strategy

it follows that:

$$\begin{aligned} t_k &= \frac{q}{N_{\mathrm{tot}}} \sum_{i=1}^{m} \sum_{j=1}^{m} t^{(j)} \\ &= \frac{q}{N_{\mathrm{tot}}} m\, t^{(\mathrm{ref})} \end{aligned} \tag{9}$$

in which $t^{(\mathrm{ref})} = \sum_{j=1}^{m} t^{(j)}$ is the total reference time per individual. With $N_{\mathrm{tot}} = \mathrm{const}$, the number of completed simulation n_{sim} in the time interval $t^{(\mathrm{ref})}$ is constant:

$$\begin{aligned} n_{\mathrm{sim}} &= t^{(\mathrm{ref})} / (q\, t_k) \\ &= N_{\mathrm{tot}} / m \end{aligned} \tag{10}$$

Therefore, even in the case of sequential optimization, the utilization of the resources was maximized. Note that when $q > 1$, the strong scaling efficiency improves because the number of parallel processes in each CFD simulation is reduced for a fixed CPU budget. However, this can be compensated for by the higher probability of waiting time in queue in the computing server if running without reservation, as the number of concurrent jobs increases.

3 Results

3.1 Initial Design Space Exploration. Before performing a direct optimization of the intake geometry, the design space was explored with a DoE to investigate the correlation between the chosen decision variables and the performance metrics, under the two operating conditions. In fact, the choice of the formal optimization problem must adhere to the physics involved and to the nature of the objectives. The DoE was conducted with a sample of 300 quasi-random individuals generated from a Sobol set that were simulated with the parallel strategy described above with $q = 4$. The distribution of performance metrics is analyzed in Fig. 7.

At takeoff, the total pressure loss $1 - \mathrm{IPR}$ correlates linearly with the $\mathrm{DC}(60)$ index, Fig. 7(*a*), indicating that these two metrics are strongly linked, as can be expected from the definition of $\mathrm{DC}(60)$, which is proportional to the average total pressure of the AIP. Taking $\mathrm{DC}(60) = 0.10$ as the upper limit, the inlet pressure losses must be less than 0.7%. Clearly, $\mathrm{DC}(60)$ is insensitive to some distortion patterns and is zero even in a flow with no incidence, since it does not recognize the boundary layer losses in an axisymmetric flow field. Therefore, for $1 - \mathrm{IPR} < 0.4\%$, $\mathrm{DC}(60)$ remains almost constant, meaning that it is a significant indicator in the presence of a sufficiently developed distortion, but it is incapable of discriminating between good intakes with no appreciable separation. The total pressure loss also exhibits a linear correlation with $\widetilde{D}_{\dot{m}}(p^0)$, which basically replicates the behavior of $\mathrm{DC}(60)$, but now with the advantage that being an integral metric it can recognize any possible distortion pattern and changes in the boundary layer region itself. Therefore, the optimization objective at takeoff was established as a linear combination of the two distortion indices with the weights chosen to give a similar sensitivity to IPR, according to the outcome of this DoE. Minimizing f_1 (Eq. (6)) will thus ensure to minimize also the total pressure loss, capturing the occurrence of a generic distortion pattern causing either a deterioration of the boundary layer flow, relative to the reference condition upon which $\widetilde{D}_{\dot{m}}(p^0)$ is based, or a substantial flow separation.

Figure 7(*b*) reports the isentropic axial thrust produced by the fan stream, which is also affected by the IPR according to its definition. $C_{F,x}$ saturates as IPR recovers to one. At the same time, also the normalized total pressure ratio of the fan, measured from the AIP to the exit of the fan, increases. The total pressure of the nozzle is thus $p_0^0 \times \mathrm{IPR} \times \mathrm{TPR}$ and benefits from the contemporary improvement in both the intake performance and the fan compression, resulting in an increased thrust coefficient.

In addition to total pressure distortion, short intakes suffer from reduced flow strengthening capability, manifesting as flow swirl at

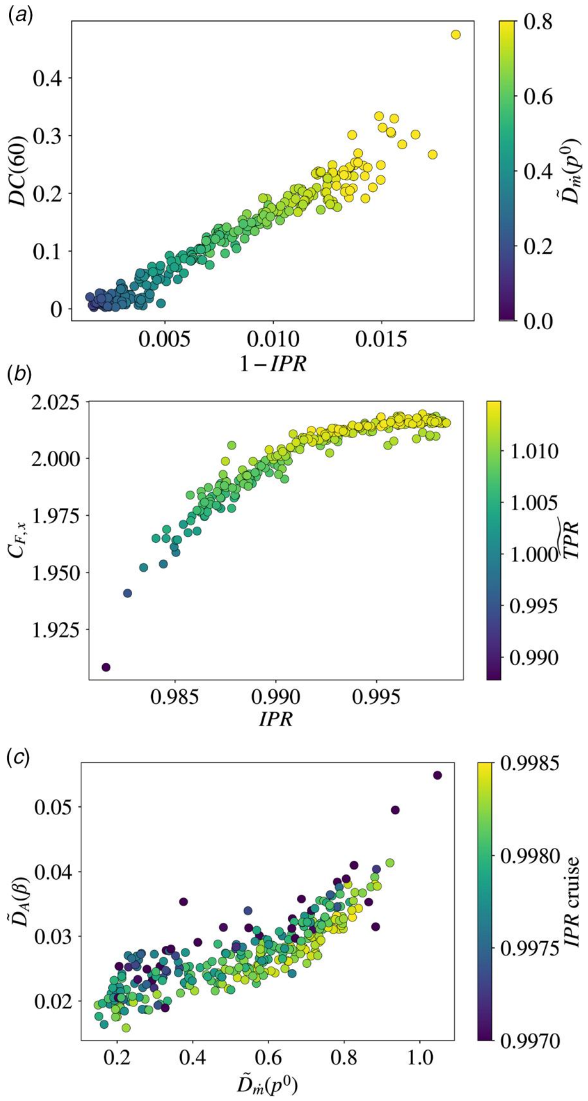

Fig. 7 Performance metrics correlations in DOE: (*a*) total pressure losses and DC(60) at take-off, (*b*) IPR and thrust coefficient at take-off, and (*c*) total pressure and incidence distortion

the fan face. The relative flow angle, or equivalently the incidence distortion index $\widetilde{D}_A(\beta)$ versus the same distortion index on total pressure $\widetilde{D}_{\dot{m}}(p^0)$ is shown in Fig. 7(*c*). Here, the distribution is nonlinear but monotonic, with incidence distortion growing along with the total pressure one. These metrics are now compared against cruise IPR, showing the rationale for the multi-objective optimization, i.e., that figure of merit tends to improve for higher distortion levels at takeoff. As expected, very different flow fields from low to high speed and from high to low incidence require substantially different geometries to avoid strongly adverse effects, resulting in a conflicting trend between the takeoff and the cruise performance.

In addition to the correlation between the performance metrics, the role of the design variables in affecting these indices is also important. To determine their influence, two common feature selection algorithms for regression were used: the F-test [44] and the maximum relevance minimum redundancy method [45]. The results are shown in Fig. 8, with six global size variables and six local variables ζ_i that affect the position of the intake lip and the B-splines control points of the diffuser. At takeoff, Fig. 8(*a*), the two tests gave similar indications: the most important variables affecting $\widetilde{D}_{\dot{m}}(p^0)$ are the highlight radius, the keel contraction ratio CR_{180} and the aspect ratio AR_{180}, and the scarf angle σ. This can be explained by the much higher susceptibility to separation for the flow past the keel, caused by the angle of attack, opposed to the crown, where despite MFCR > 1, the flow is able to circumvent the nose without detaching from the body. in cruise, the two tests returned a different importance for IPR, with the F-test setting ζ_2 as the most influential variable (it controlled the local curvature of the intake lip between the highlight and the throat), followed by AR_0, with no influence for the remaining variables. The maximum relevance minimum redundancy algorithm indicated only the contraction ratio as an influential feature. The importance of the contraction ratio can be attributed to its effect on the angle of the wall diffuser, which also depends on the aspect ratio. This outcome suggests that not all geometric variables might be necessary to predict the response. However, they are certainly necessary to fully specify the geometry in the given parametrization. In addition, the Kriging regressor possesses an embedded feature selection capability as part of the model learning process, thus redundant features are inherently given a lower weight and can be retained as decision variables.

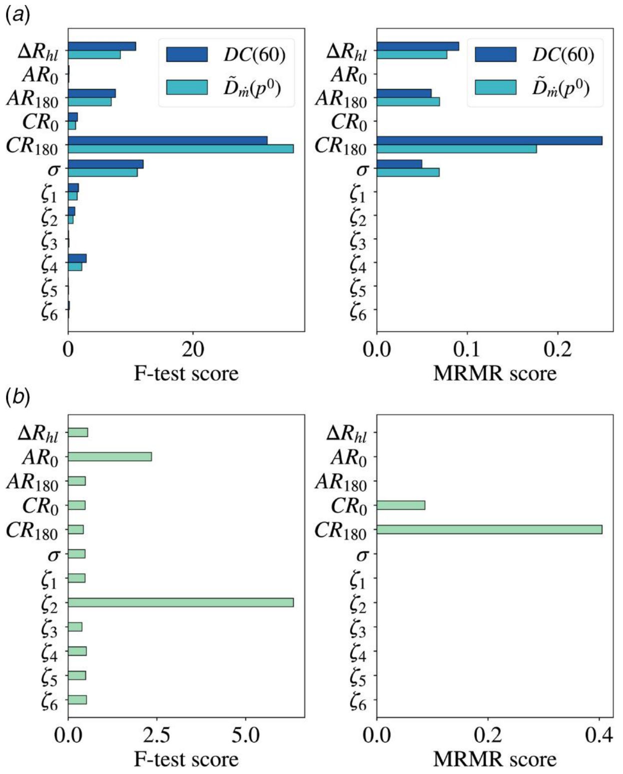

Fig. 8 Feature importance in DOE at the two considered operating conditions: (*a*) take-off and (*b*) cruise

The impact of azimuthal contouring on takeoff performance was evaluated more in-depth for a number of representative geometries selected among the DoE pool. To do that, the design variables controlling the distribution of the contraction ratio and aspect ratio over the circumferential direction were changed parametrically to produce three variants for each of the 20 selected shapes. Letting $\theta_l \in [0,1]$ being an index of the azimuthal variability and ν denoting either *CR* or *AR*, the original crown parameters were modified as

$$\nu_0^{\mathrm{new}} = \theta_l \nu_0^{\mathrm{old}} + (1-\theta_l)\nu_{180}^{\mathrm{old}} \tag{11}$$

with $\theta_l = [0, 0.5, 1]$. Therefore, θ_l indicates whether the intake kept the original azimuthal distribution ($\theta_l = 1$), had the crown profile equal to the keel ($\mathrm{CR}_0 = \mathrm{CR}_{180}$ and $\mathrm{AR}_0 = \mathrm{AR}_{180}$), or had the crown profile as the average between the keel and the original values. Note that the droop and the scarf angles did not change, thus maintaining in any case a three-dimensional shape. Figure 9 shows the results at takeoff, reporting IPR and DC(60) against the 3D level. For each line, representing an intake variation, the maximum IPR is marked with a green circle. Overall, both metrics tend to improve for

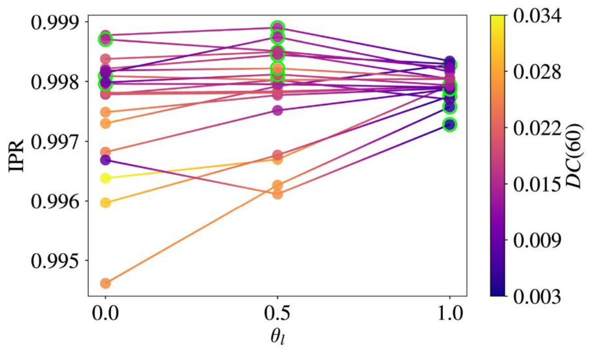

Fig. 9 Effect of inlet lip three-dimensionality at takeoff

shapes with an azimuthal contouring. A quarter of the cases (5/20) show the best IPR (and DC(60), for the reason explained above), with the crown being a mix of the original intake, $\theta_l = 0.5$. Only $3/20 = 15\%$ of the individuals exhibit better values with constant lip parameters, while $12/20 = 60\%$ perform better with the original version. The assessment confirms that it is worth controlling how intake parameters vary along the circumference to smoothly adapt the geometry to the more severe conditions that arise near the bottom dead center at high incidence.

3.2 Intake Optimization. From the analysis of the DoE data, the multi-objective and multipoint optimization problem could be formulated as stated in Eq. (6). The final Pareto frontier in the objective function space is reported in Fig. 10, which shows the evolution of the sampling throughout the iterations. The solver clustered many points in the lower left corner of the Pareto frontier, where the potential for improving both objectives is maximum. The final front features a larger variation in the takeoff objective f_1, reaching values greater than 0.1, which are associated with the inlet separation. In cruise, the total pressure loss range, measured by f_2, is instead more limited, roughly between 0.15% and 0.20%. The conflicting nature of the objectives, already highlighted in the DoE analysis, can now be better understood. Inlets with the best cruise performance are highly penalized at high incidence and are likely to produce separation.

The shapes found on the Pareto front are shown in Fig. 11. Figure 11(*a*) reports the azimuthal distribution of the intake lip parameters, from which a certain pattern can be observed going along the Pareto from left to right, at increasing values of f_1. The best takeoff shapes tend to have a higher CR_{180} and a lower CR_0, with less variation of *AR* and a lower scarf angle. This is in agreement with the parametric analysis in Ref. [34] and can be appreciated from the sectional views in Figs. 11(*b*) and 11(*c*), where the first also shows that the highlight radius reduces as f_1 grows. This outcome is significant because it indicates that the optimization has captured a physical trend in placing points on the Pareto front. This trend can be examined with the help of the isentropic Mach number distribution

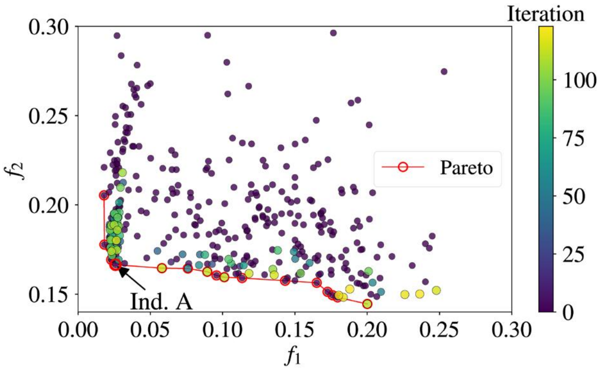

Fig. 10 Pareto front of multi-objective optimization

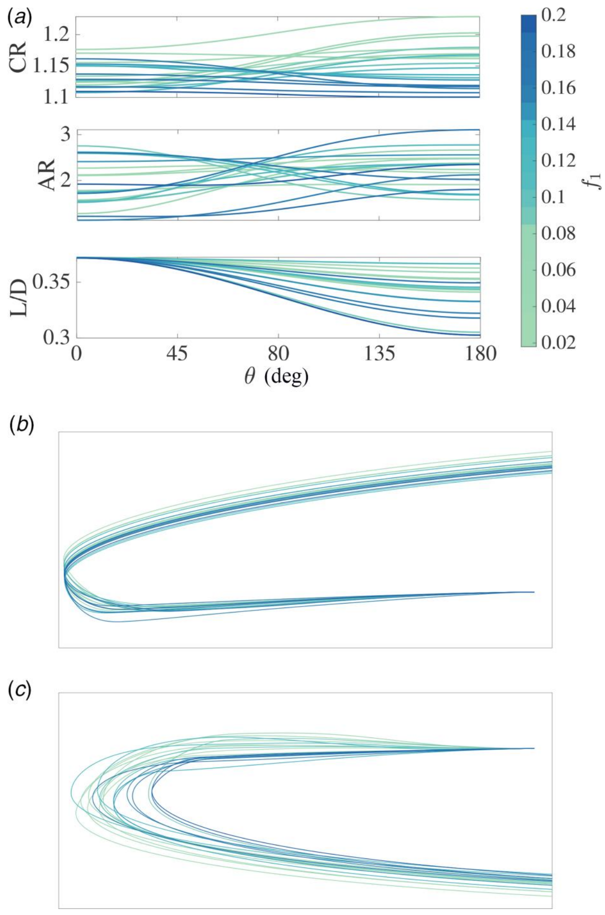

Fig. 11 Geometric shapes on Pareto frontier: (*a*) azimuthal distribution of geometric variables, (*b*) crown geometries, and (*c*) keel geometries

$M_{\mathrm{iso}} = \sqrt{\frac{2}{\gamma-1}\left[\left(\frac{p_\infty^0}{p}\right)^{(\gamma-1)/\gamma} - 1\right]}$ on the nacelle symmetry plane at takeoff, in Fig. 12. Recalling that along the Pareto front low f_1 indicates better takeoff performance and low f_2 better cruise performance, and that the two objectives have opposite trends, on the crown there is no noticeable correlation between the surface Mach number and the takeoff objective. On the keel, the higher highlight radius for the best takeoff geometries reduces MFCR and puts the stagnation point closer to the highlight, shortening the flow path to enter the inlet. However, the level of diffusion is higher when f_1 is small, due to the greater CR_{180} producing an enlarged diffuser angle, but this is compensated for by the lower scarf angle, which generates longer intakes on the bottom side. Moreover, the diffusion occurs more gently than in high f_1 geometries which fall on the leftmost Pareto edge and exhibit poorer takeoff performance but better cruise characteristics. For these latter individuals the pressure recovery after the supersonic isentropic Mach number occurs sharply and causes separation, recognizable by the flat M_{iso} profile.

The Mach number itself thus exhibits regularity across Pareto, as depicted in Fig. 13. Progressing along the Pareto front from left (best takeoff, low f_1, high f_2) to right (best cruise, high f_1, low f_2), the average and maximum surface Mach number decrease, showing that optimal low-speed performance is associated with a higher suction peak terminated by a shock-wave. In cruise, geometries with lower values of the f_2 objective and thus reduced total pressure losses have a decreased maximum and average M_{iso} due to the lower contraction ratio, which limits the boundary layer diffusion.

3.3 Further Assessment for Selected Geometries. Some individuals on the Pareto front of the optimization were selected

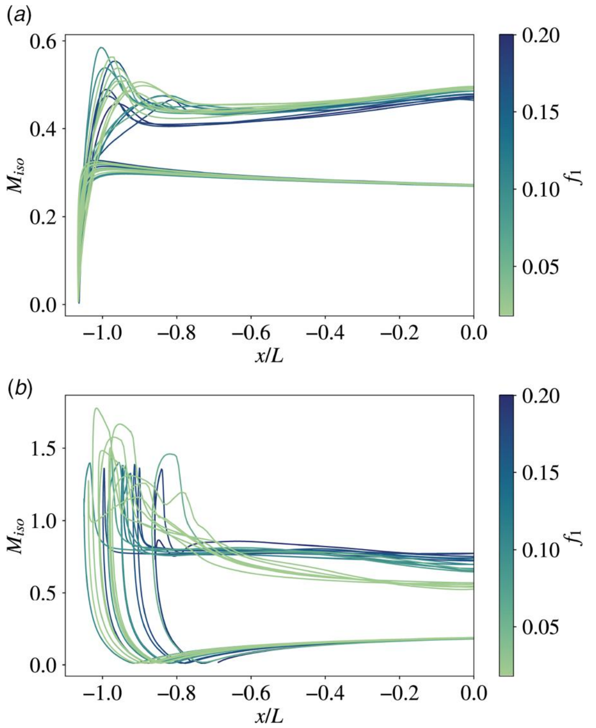

Fig. 12 Isentropic Mach number distribution for Pareto points at takeoff: (*a*) crown and (*b*) keel

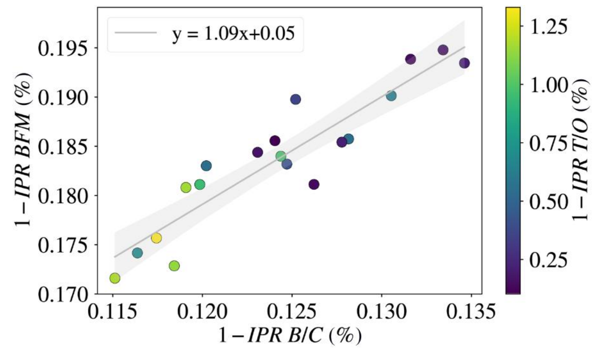

Fig. 14 Correlation between cruise performance with different modeling approaches

for further evaluation on the modeling approach and additional operating conditions.

3.3.1 Effect of Engine Modeling in Cruise. The first analysis investigated the validity of the engine modeling approach adopted for cruise simulations, with a mass flow outlet boundary condition set in a half-model nacelle with a pressure outlet boundary condition, which neglected the effect of the fan on the flow field. To this purpose, the geometries on the Pareto frontier were resimulated using the full annulus nacelle and the BFM, now including the complete fan with OGV stage and the core inlet duct, where a radial equilibrium pressure outlet boundary condition was set, to give the design bypass ratio. The result of the investigation is summarized in Fig. 14, showing the dispersion chart between the total pressure loss evaluated with the nacelle with Boundary Conditions B/C model as in the optimization, and the same value computed with the full stage BFM. The points exhibit a linear correlation, the regression line shown in the figure having an offset of 0.05% and a slope of 1.09. This outcome shows that the losses in the boundary layer are higher when the fan is present, but the relationship can be approximated as linear. Therefore, although less accurate, the method used in the optimization remains valid and affordable.

3.3.2 Sensitivity to the Angle of Attack at Take-Off. From the Pareto front of the optimization, six geometries approximately equispaced in f_1 were selected to further assess their sensitivity to the angle of attack. In fact, the optimization was run at constant incidence, but depending on the shape, each nacelle has a different tolerance to the angle of attack. Figure 15(*a*) shows the variation of

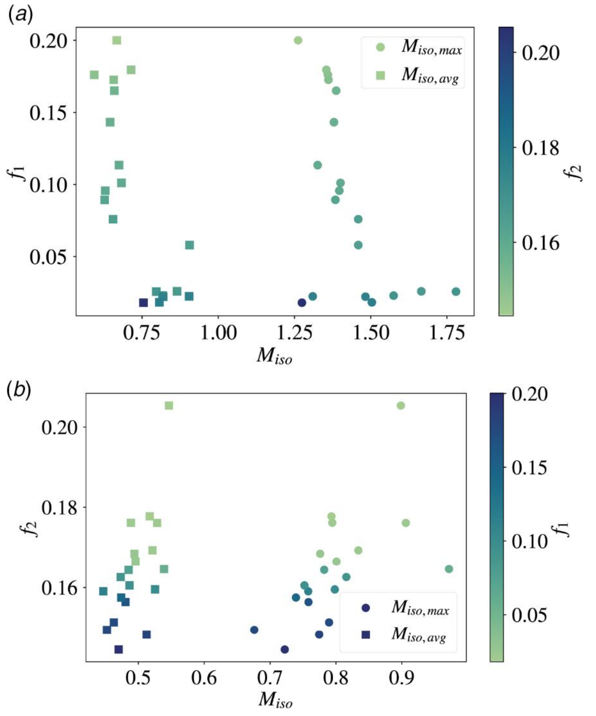

Fig. 13 Isentropic Mach number statistics for Pareto points: (*a*) take-off and (*b*) cruise

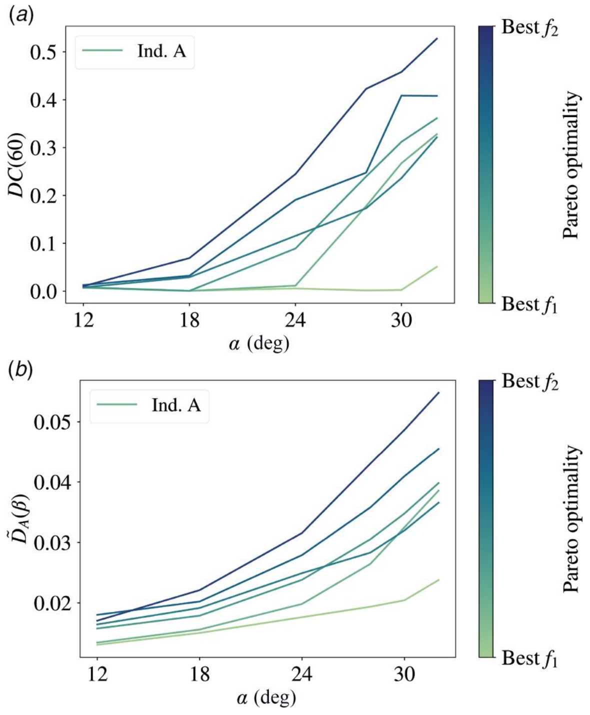

Fig. 15 Performance metrics variation for selected Pareto points in takeoff polar: (*a*) DC (60) and (*b*) $D_A(\beta)$

Table 2 Comparison of integral metrics between URANS and BFM

Case	$\tilde{\dot{m}}_c$	ΔTPR	$\Delta\eta_{iso}$	IPR
URANS	0.963	0.019	−0.005	0.996
BFM	0.959	0.023	−0.028	0.997

(a) $\alpha = 24$ deg

Case	$\tilde{\dot{m}}_c$	ΔTPR	$\Delta\eta_{iso}$	IPR
URANS	0.945	0.0	−0.028	0.987
BFM	0.950	0.016	−0.033	0.988

(b) $\alpha = 28$ deg

Variations expressed relative to the design condition.

the DC(60) index versus the angle of attack α for the six geometries. The stall angle of the intake, coinciding with its separation and the rapid growth of DC(60), regularly increases moving along the Pareto from best $f_2 =$ cruise to best $f_1 =$takeoff, ranging from 16 deg for the best in cruise, to 32 deg for the base in takeoff. This analysis can be helpful in selecting a geometry from the Pareto frontier based on the high-incidence requirements for the intake, and it underpins the strong conflict between the design attributes for optimal cruise and optimal high-incidence high-thrust operation. Interestingly, the total pressure distortion appears to be strongly correlated with the swirl distortion, as shown in Fig. 15(*b*). $\widetilde{D}_A(\beta)$ has a positive offset and a progressively higher sensitivity to the angle of attack for shapes exhibiting a better cruise performance, which is consistent with the DoE result of Fig. 7(*c*), where the total pressure and incidence distortion were found to have a positive nonlinear correlation.

3.4 Detailed Flow Coupling Analysis. The sensitivity to the angle of attack was used to select an individual from the Pareto point in which to conduct further detailed investigation of the coupling between the turbomachinery and the intake flow by means of unsteady rotating mesh simulations, also allowing further validation of the adopted BFM formulation under distortion. Specifically, the Pareto point indicated as Ind. A in Fig. 10 and in Fig. 15 was chosen, having an inlet stall angle of 28 deg and exhibiting a good balance between the two objectives.

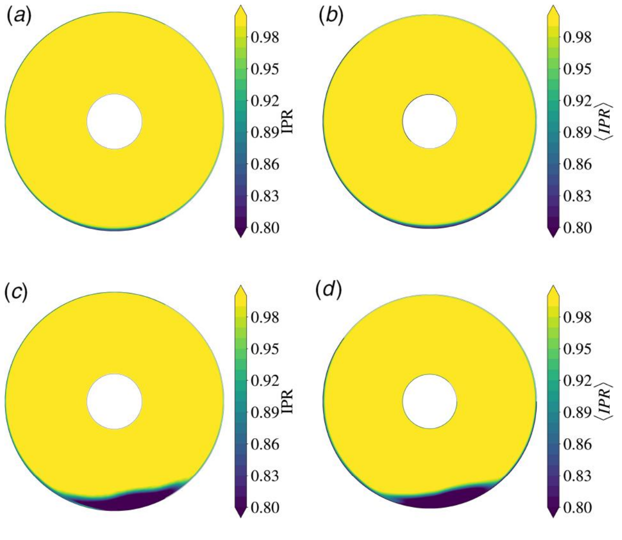

Fig. 16 AIP local inlet pressure recovery comparison between time-averaged URANS and BFM at two angles of attack: (*a*) BFM, $\alpha = 24$ deg, (*b*) URANS, $\alpha = 24$ deg, (*c*) BFM, $\alpha = 28$ deg, and (*d*) URANS, $\alpha = 28$ deg

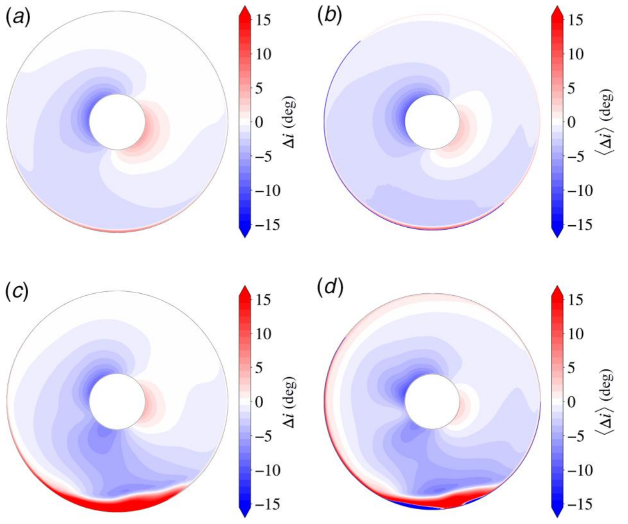

Fig. 17 AIP incidence change comparison between time-averaged URANS and BFM at two angles of attack: (*a*) BFM, $\alpha = 24$ deg, (*b*) URANS, $\alpha = 24$ deg, (*c*) BFM, $\alpha = 28$ deg, and (*d*) URANS, $\alpha = 28$ deg

First, the integral performance parameters between the URANS averaged data and the BFM simulations are compared in Table 2, where the corrected inlet mass flowrate is normalized with the reference design value, and the difference in TPR and isentropic efficiency is calculated equally from the design value of the fan. The body force model closely replicates the performance at $\alpha = 24$ deg. The slightly lower isentropic efficiency is consistent with the clean case characteristic shown in 5(*b*). At $\alpha = 28$ deg, integral metrics under distortion are again in good agreement, although the BFM predicts a lower decrease in TPR and efficiency compared to the URANS, while matching IPR.

Aerodynamic Interface Plane distributions are shown in Figs. 16 and 17. As reported in the previous table, the local inlet pressure ratio in Fig. 16 is in very good agreement between the two models, indicating that the averaged inflow conditions resulting from the coupling between the inlet separation and the rotor are physically reproduced by the BFM. Figure 17 illustrates the local change in rotor incidence relative to a clean ducted case with equal corrected mass flowrate and rotational speed. The distributions at $\alpha = 24$ deg have close local features around the spinner, where the flow circumvention induces co- and counterswirl, and also near the hub at the keel, where the boundary layer thickness is increased. After the inlet has separated at $\alpha = 28$ deg, the consistency of the BFM remains high, with a minor deviation near the shroud around the annulus, where the average flow field of the URANS has a higher local incidence change.

Downstream of the rotor, the azimuthal distribution of relevant metrics at different span values $\tilde{r} = (r - r_{\text{hub}})/(r_{\text{shroud}} - r_{\text{hub}})$ is reported in Fig. 18. The total pressure increase across the rotor is nonuniform due to the presence of inlet swirl and total pressure distortion. The mass flux redistribution on the fan face resulting from the streamtube rotation and the radial velocity components causing nonhomogeneous static pressure introduce a downstream total pressure variation also in lower span regions not involved in the flow separation. At $\tilde{r} = 0.10$, a long azimuthal wavelength modulation caused by streamtube rotation coexists with a shorter azimuthal wavelength distortion originating from the flow prerotation of circumvention of the spinner. These two effects are well replicated by the BFM and are also present at higher span values, where they sum up to the shorter azimuthal length-scale modulation in the distortion core at $\tilde{r} = 0.9$. Here, the URANS averaged distribution exhibits an initial total pressure drop, followed by a high compression peak at $\theta = 250$ deg and additional oscillations. The BFM overpredicts the initial total pressure drop at $\theta = 225$ deg,

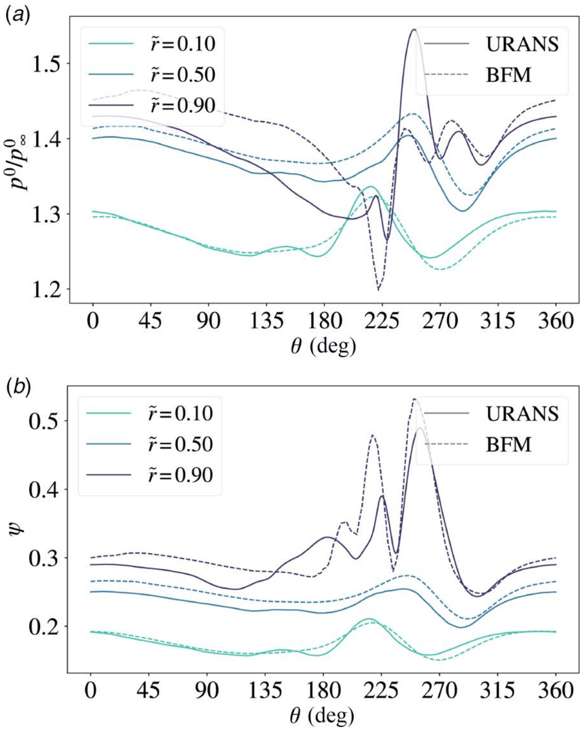

Fig. 18 Circumferential distribution of time-averaged URANS and BFM data at rotor outlet: (*a*) TPR and (*b*) work coefficient

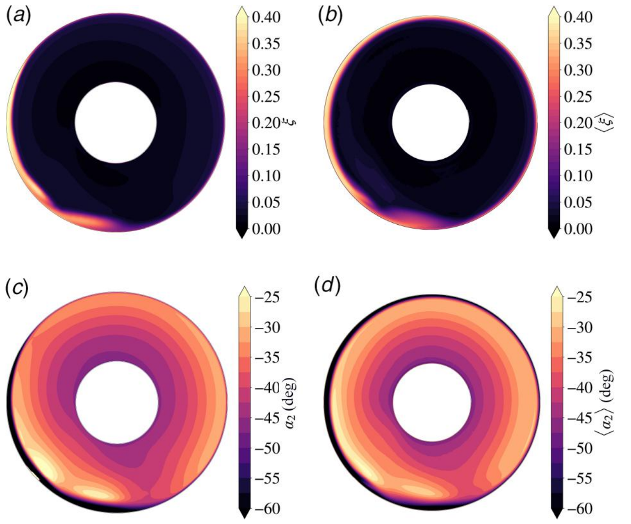

Fig. 19 Comparison between time-averaged URANS and BFM data at rotor outlet: (*a*) BFM, entropy function, (*b*) URANS, entropy function, (*c*) BFM, absolute swirl angle, and (*d*) URANS, absolute swirl angle

failing to generate the large compression peak at $\theta = 250$ deg. However, it correctly reproduces the waviness of the distribution, the phase of the local extrema, and the value of those that occur from $\theta = 270$ deg to $\theta = 300$ deg, indicating good replicability of the physical mechanisms of distortion transfer across the cascade.

Work input is evaluated by means of the work coefficient $\psi = \Delta H^0/U^2$, in which H^0 is the mass-weighted average total enthalpy. Its distribution in Fig. 18(*b*) mimics the aforementioned total pressure. Up to midspan and outside the distortion core, the BFM closely duplicates the averaged URANS data, with both showing an oscillatory behavior from $\theta = 180$ deg to $\theta = 315$ deg caused by the swirl components of the flow circumventing the spinner. Within the flow separation, the BFM captures the change in enthalpy starting from $\theta = 225$ deg, whereas the two peaks of URANS near $\theta = 180$ deg and $\theta = 220$ deg differ in amplitude and position, although qualitatively present.

The correlation between the compression achieved and the work input is related to the losses occurring throughout the cascade, which are visualized by means of the entropy loss function $\xi = 1 - e^{-(s_2 - s_1)/R}$ at the rotor outlet in Figs. 19(*a*) and 19(*b*). The high-loss region develops near the casing due to the blade interaction with the recirculation, and it is qualitatively reproduced by the body force model through the parallel force. The evolution of the flow in URANS differs in the tip region beyond the separation, with an area of high entropy generation that extends further circumferentially compared to the BFM. The latter does not model the tip leakage flow, where there is no force, and therefore is unable to replicate the evolution of the vortical structures that are found in URANS, which can explain the lower efficiency drop predicted upon separation.

The absolute swirl angle distribution of Figs. 19(*c*) and 19(*d*) presents the same difference near the casing, with a higher work input found in URANS. Apart from this region, the consistency between the two methods remains high, and the local variations of swirl angle are well simulated by the BFM.

The flow field of the cascade is heavily perturbed near the tip region, as it can be seen in Fig. 20(*a*), showing the instantaneous entropy function or URANS at the span value $\tilde{r} = 0.95$. The machine rotation in the figure is from left to right. The highest losses are generated in the blades leaving the distortion core, where the passage is blocked by massive suction side separation, with incipient flow spillage visible in one blade passage. The large recirculation propagates across half of the circumference, determining higher unsteadiness downstream of the cascade and increased mixing near the tip, as previously observed in Fig. 19(*b*). The intake separated region is attenuated by the fan suction that induces a flow contraction starting from around two axial chords upstream of the leading edge. The BFM flow field at the same span is shown in Fig. 20(*b*). The BFM has a single high loss region originating from the interaction of the blades with the distortion, as flow detachment over the blade surfaces, as well as tip leakage are not physically modeled. However, although more confined and with a lower circumferential extension, the entropy generation and the interaction of the detached boundary layer past the intake with the blades appear to be consistent with the URANS.

The characteristics of the inlet flow resulting from the coupling with the fan are further examined below, starting from the analysis of the axial skin friction coefficient $C_{f,z} = \tau_Z/0.5\rho V_\infty^2$ that reveals the area of flow separation at $\alpha = 28$ deg. Figure 21 compares BFM with time-averaged URANS data in the unwrapped inlet surface, where the abscissa represents the angular coordinate and the ordinate the normalized axial position, in which $z = 0$ lies on the AIP. The flow separation, indicated by the negative skin friction coefficient, originates near the leading edge of the inlet lip on the keel and progresses toward the fan, where the effect of suction of the rotor draws the fluid, altering its symmetry and generating the previously analyzed response of the cascade. The development of flow recirculation and its extension are well matched in the body force model, where the start of the separation and the topology are very close to URANS, and minor deviations appear as a result of the unsteady pressure field of the fan blades, which is not modeled.

By analyzing the streamwise gradient of static pressure, the phenomenology of the flow separation and the accuracy of the BFM can be further assessed. In Fig. 22, the development of the flow past the intake can be clearly appreciated. Due to MFCR > 1, the stagnation point is on the external cowl throughout the circumference, inducing acceleration of the flow with an initially favorable pressure gradient. Around the bottom dead center at $\theta = 180$ deg, the acceleration triggers a shock wave which is the cause of boundary layer detachment, visualized by the high positive streamwise pressure gradient. Past the shock wave, the separated flow has a low pressure gradient, whereas the attached flow surrounding the separation bubble has modest diffusion under a positive pressure

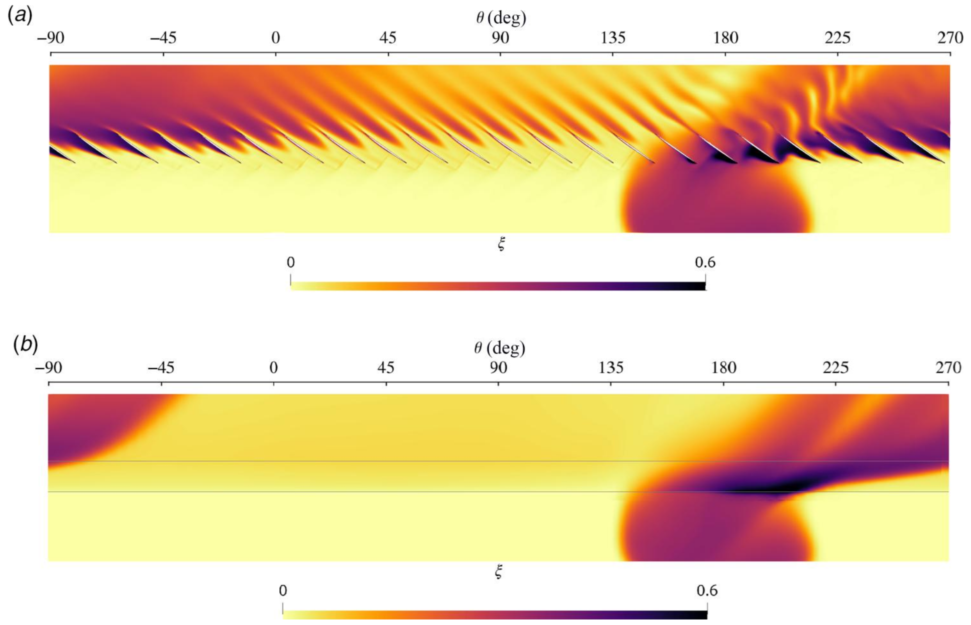

Fig. 20 Entropy generation across the cascade at $\tilde{r}=0.95$ and $\alpha=28$ deg: (*a*) URANS and (*b*) BFM

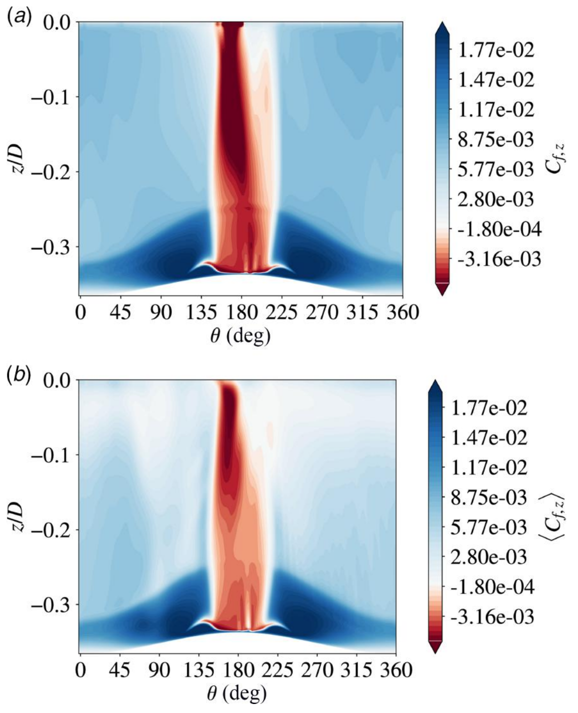

Fig. 21 Comparison of intake surface axial skin friction coefficient for URANS and BFM at $\alpha=28$ deg: (*a*) BFM and (*b*) URANS

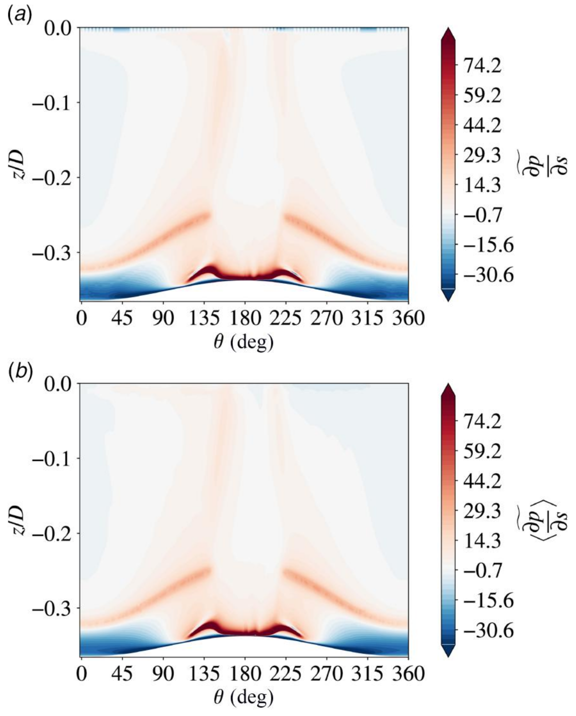

Fig. 22 Comparison of normalized intake surface streamwise pressure gradient for URANS and BFM at $\alpha=28$ deg: (*a*) BFM and (*b*) URANS

gradient. This structure is very well replicated in the BFM, thanks to the matching of MFCR and the flow redistribution on the AIP.

The phase-locked average of the URANS data over the inlet highlights the coupling between the rotating pressure field of the rotor propagating upstream and the inlet boundary layer, reported in Fig. 23. The normalized standard deviation of the pressure pulsation reveals different phenomena. The upstream propagation of the bow shocks is largely affected by the inlet leading edge flow separation. The fan rotation is toward negative θ values in the figure. The leeward side of the intake lip shock, around $\theta = 200$ deg, has higher unsteadiness, compared to the windward side, which is induced by the interaction with the blade shocks that are able to cross the separated region. In contrast, the recirculation core appears to be rather stable over time. Shock waves emerging from the distortion core, from $\theta = 180$ deg to $\theta = 150$ deg, are unable to reach the inlet leading edge, and the direction of propagation is more axial, because of the different operating conditions of the blade passages and the standing shock inclination. Due to the highly distorted flow shown in Fig. 20(*a*), blades leaving the distortion core generate increased shock unsteadiness, which is visible by the higher standard deviation of traces emerging from $\theta = 90$ deg to $\theta = 45$ deg. These are drawn toward the separated region, indicating substantial flow migration over the intake surface.

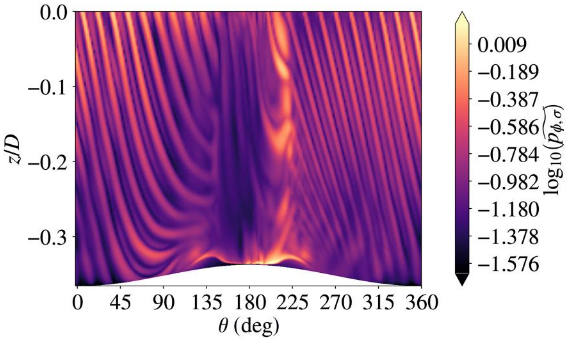

Fig. 23 Phase-locked standard deviation of intake surface pressure from URANS simulation at α=28 deg

4 Conclusions

The research has investigated the coupling between a low pressure ratio transonic fan of an ultrahigh bypass ratio turbofan and a short aero intake with different methods, focusing on the intake design and the modeling of the turbomachinery. The analysis of the intake design attributes and their influence under mutual interaction with the rotor has been first studied by means of a body force model at high thrust, high incidence. From the point of view of the short aero-intake design, the study highlights these main points:

- The intake performance in cruise and take-off conditions exhibits a strong conflicting dependency upon its geometric parameters, which makes a multi-objective and multi-point design with three-dimensional features necessary to ensure high cruise efficiency with adequate off-design characteristics.
- Total pressure losses during take-off have a positive linear correlation with total pressure distortion and a nonlinear correlation with swirl distortion and thrust coefficient.
- Optimal take-off shapes tend to have a higher contraction ratio on the keel and a lower scarf angle. The isentropic Mach number on the lower lip is generally higher, which is associated with a leading edge shock wave that does not cause flow detachment. The lip stall at higher incidence is triggered by the shock wave.
- Optimal cruise shapes have lower intake diffusion and contraction ratio values, reducing the losses of the boundary layer. Integral cruise performance can be reasonably estimated using a throughflow nacelle in the absence of inlet distortion.

The detailed assessment of the flow topology and the comparison between the body force model of the fan with URANS simulations at high incidence have further validated the simplified modeling approach, reaching these main conclusions:

- The integral performance metrics of the fan predicted by the BFM are in good agreement with the averaged URANS data, even with distortion. The inlet flow status and the total pressure distribution on the AIP are very well matched, indicating a consistent physical reproduction of the flow redistribution imposed by the fan.
- The fan response to inlet distortion of the BFM generally agrees with URANS. The main spatial length scales of the flow field downstream of the rotor are captured, with larger deviations in areas of strong flow separation, where the agreement is qualitatively acceptable. Major deviations are found near the tip, where leakage flow phenomena are not modeled in the BFM.
- The fan/intake coupling is consistent over the inlet surface, with the origin of flow separation at high incidence, its development along the duct, and its attenuation upstream of the fan well replicated by the BFM.

In conclusion, the study has developed a novel three-dimensional short aero-intake design tool based on a body force model for optimization under the effect of full coupling with the fan. The adopted turbomachinery representation appears to be suitable for replicating the mutual component interaction occurring in compact nacelles of modern low-pressure ratio fans in a computationally efficient way. It can help designers investigate novel configurations and improve the estimation of turbomachinery performance under installation, which requires a physically consistent modeling of the complex interaction occurring.

Acknowledgment

The author acknowledges the CINECA award under the ISCRA initiative for the availability of high performance computing resources and support.

Data Availability Statement

The datasets generated and supporting the findings of this article are obtainable from the corresponding author upon reasonable request.

Nomenclature

AR = aspect ratio
B/C = boundary conditions
BFM = body force model
C_f = skin friction coefficient
C_F = force coefficient
CR = contraction ratio
D = fan diameter
$\widetilde{D}_c(\phi)$ = distortion index of ϕ with c-average
DC(60) = distortion criterion
f = fitness function
H = enthalpy
i = incidence
IPR = inlet pressure ratio
L = intake length
M = Mach number
$\dot{m}$ = mass flow rate
p = pressure
q = dynamic pressure
R_{hl} = highlight radius
s = entropy
T = temperature

Greek Symbols

α = angle of attack, absolute swirl angle
β = relative swirl angle
γ = specific heat ratio
ζ = B-spline parameter
η_{iso} = efficiency
ξ = entropy function
σ = scarf angle
τ_z = axial wall shear stress
ψ = work coefficient

Superscripts and Subscripts

AIP = aerodynamic interface plane
iso = isentropic
∞ = free stream value
$\widetilde{\cdot}$ = normalized value
$\bar{\cdot}$ = area-averaged value
$\langle\cdot\rangle$ = time-averaged value
$\langle\cdot\rangle_\sigma$ = standard deviation
0 = stagnation value
1 = rotor inlet
2 = rotor outlet

References

[1] Benzakein, M. J., 2014, "What Does the Future Bring? A Look at Technologies for Commercial Aircraft in the Years 2035–2050," Propul. Power Res., **3**(4), pp. 165–174.

[2] Abu Salem, K., Palaia, G., Bravo-Mosquera, P. D., and Quarta, A. A., 2024, "A Review of Novel and Non-Conventional Propulsion Integrations for Next-Generation Aircraft," Designs, **8**(2), p. 20.
[3] Kennedy, S., Robinson, T., Spence, S., and Richardson, J., 2014, "Computational Investigation of Inlet Distortion at High Angles of Attack," J. Aircr., **51**(2), pp. 361–376.
[4] Cao, T., Vadlamani, N. R., Tucker, P. G., Smith, A. R., Slaby, M., and Sheaf, C. T., 2017, "Fan-Intake Interaction Under High Incidence," ASME J. Eng. Gas Turbines Power, **139**(4), p. 041204.
[5] Vadlamani, N. R., Cao, T., Watson, R., and Tucker, P. G., 2019, "Toward Future Installations: Mutual Interactions of Short Intakes With Modern High Bypass Fans," ASME J. Turbomach., **141**(8), p. 081013.
[6] Mohankumar, B., Hall, C. A., and Wilson, M. J., 2021, "Fan Aerodynamics With a Short Intake at High Angle of Attack," ASME J. Turbomach., **143**(5), p. 051003.
[7] Mohankumar, B., Hall, C. A., and Wilson, M. J., 2021, "Sweep Effects on Fan-Intake Aerodynamics at High Angle of Attack," ASME Paper No. TURBO-21-1211.
[8] Gunn, E. J., Brandvik, T., and Wilson, M. J., 2021, "Fan-Intake Coupling With Conventional and Short Intakes," ASME Paper No. GT2021-58829.
[9] Coschignano, A., and Babinsky, H., 2019, "Boundary-Layer Development Downstream of Normal Shock in Transonic Intakes at Incidence," AIAA J., **57**(12), pp. 5241–5251.
[10] Lee, K.-B., Wilson, M., and Vahdati, M., 2019, "Effects of Inlet Disturbances on Fan Stability," ASME J. Eng. Gas Turbines Power, **141**(5), p. 051014.
[11] Boscagli, L., Christie, R., MacManus, D., and Piovesan, T., 2022, "Aerodynamics of a Short Intake in Crosswind," Aerosp. Sci. Technol., **129**, p. 107826.
[12] Boscagli, L., MacManus, D., Christie, R., and Sheaf, C., 2024, "Effect of Unsteady Fan-Intake Interaction on Short Intake Design," ASME J. Eng. Gas Turbines Power, **146**(3), p. 031008.
[13] Burlot, A., Sartor, F., Vergez, M., Méheut, M., and Barrier, R., 2018, "Method Comparison for Fan Performance in Short Intake Nacelle," AIAA Paper No. 2018-4204.
[14] Stuermer, A., 2019, "DLR TAU-Code uRANS Turbofan Modeling for Aircraft Aerodynamics Investigations," Aerospace, **6**(11), p. 121.
[15] Meheut, M., Sartor, F., Vergez, M., Laban, M., Schnell, R., Stuermer, A. W., and Lefevre, G., 2019, "Assessment of Fan/Airframe Aerodynamic Performance Using 360° uRANS Computations: Code-to-Code Comparison Between ONERA, DLR, NLR and Airbus," AIAA Paper No. 2019-0582.
[16] Godard, B., De Jaeghere, E., Ben Nasr, N., Marty, J., Barrier, R., and Gourdain, N., 2017, "A Review of Inlet-Fan Coupling Methodologies," ASME Paper No. GT2017-63577.
[17] Ma, Y., Cui, J., Vadlamani, N. R., and Tucker, P., 2018, "Effect of Fan on Inlet Distortion: Mixed-Fidelity Approach," AIAA J., **56**(6), pp. 2350–2360.
[18] Carnevale, M., Wang, F., Parry, A. B., Green, J. S., and di Mare, L., 2018, "Fan Similarity Model for the Fan–Intake Interaction Problem," ASME J. Eng. Gas Turbines Power, **140**(5), p. 051202.
[19] Benichou, E., Dufour, G., Bousquet, Y., Binder, N., Ortolan, A., and Carbonneau, X., 2019, "Body Force Modeling of the Aerodynamics of a Low-Speed Fan Under Distorted Inflow," Int. J. Turbomach., Propul. Power, **4**(3), pp. 29–12.
[20] Pazireh, S., and Defoe, J., 2022, "A New Loss Generation Body Force Model for Fan/Compressor Blade Rows: Application to Uniform and Non-Uniform Inflow in Rotor 67," ASME J. Turbomach., **144**(6), p. 061005.
[21] Liu, S., Pan, T., and Li, Q., 2024, "An Improved Body Force Model to Simulate Blade Loading Variation Under Various Operating Conditions in Transonic Axial Flow Compressor," ASME J. Turbomach., **146**(10), p. 101002.
[22] Minaker, Q. J., and Defoe, J. J., 2019, "Prediction of Crosswind Separation Velocity for Fan and Nacelle Systems Using Body Force Models: Part 1: Fan Body Force Model Generation Without Detailed Stage Geometry," Int. J. Turbomach., Propul. Power, **4**(4), p. 43.
[23] Godard, B., De Jaeghere, E., and Gourdain, N., 2019, "Efficient Design Investigation of a Turbofan in Distorted Inlet Conditions," ASME Paper No. GT2019-90471.
[24] Mao, Y., and Dang, T. Q., 2020, "A Three-Dimensional Body-Force Model for Nacelle-Fan Systems Under Inlet Distortions," Aerosp. Sci. Technol., **106**, p. 106085.
[25] Awes, A., Dufour, G., Daon, R., Marty, J., Barrier, R., and Carbonneau, X., 2021, "Unsteady Body Force Methodology for Fan Operability Assessment Under Clean and Distorted Inflow Conditions," AIAA Paper No. 2021-0388.
[26] López de Vega, L., Dufour, G., and García Rosa, N., 2021, "Fully Coupled Body Force–Engine Performance Methodology for Boundary Layer Ingestion," J. Propul. Power, **37**(2), pp. 192–201.
[27] Peters, A., Spakovszky, Z. S., Lord, W. K., and Rose, B., 2015, "Ultrashort Nacelles for Low Fan Pressure Ratio Propulsors," ASME J. Turbomach., **137**(2), p. 021001.
[28] Wang, S., Cao, C., Wang, C., Wang, L., and Sun, G., 2021, "A Nacelle Inlet Design Approach With More Three-Dimensional Geometric Consideration," Aerosp. Sci. Technol., **112**, p. 106624.
[29] Silva, V. T., Lundbladh, A., Petit, O., and Xisto, C., 2022, "Multipoint Aerodynamic Design of Ultrashort Nacelles for Ultrahigh-Bypass-Ratio Engines," J. Propul. Power, **38**(4), pp. 1–18.
[30] Cao, C., Wang, S., Wang, C., Zhang, X., and Sun, G., 2022, "Nacelle Inlet Optimization at High Angles of Attack Based on the Ensemble Indicator Method," J. Aerosp. Eng., **35**(2), p. 06022001.
[31] Tao, G., Wang, W., Ye, Z., Wang, Y., Luo, J., and Cui, J., 2024, "Multi-Fidelity and Multi-Objective Aerodynamic Short Nacelle Shape Optimisation Under Different Flight Conditions," Aeronaut. J., **128**(1321), pp. 517–546.
[32] Monfaredi, M., Asouti, V., Trompoukis, X., Tsiakas, K., and Giannakoglou, K., 2023, "Aeroacoustic and Aerodynamic Adjoint-Based Shape Optimization of an Axisymmetric Aero-Engine Intake," Aerospace, **10**(9), p. 743.
[33] Yang, X., Cao, C., Wang, C., Li, L., and Sun, G., 2023, "Surrogate-Based Optimization of Nacelle Intake With Fan-Intake Interaction: Mitigating Flow Separation Under Crosswind," Aerosp. Sci. Technol., **142**, p. 108641.
[34] Magrini, A., and Benini, E., 2022, "Study of Geometric Parameters for the Design of Short Intakes With Fan Modelling," Chin. J. Aeronaut., **35**(11), pp. 18–32.
[35] ANSYS, Inc., 2022, *ANSYS Fluent User Manual*, Ansys, Inc, Canonsburg, PA.
[36] Menter, F., 1992, "Improved Two-Equation k-Omega Turbulence Models for Aerodynamic Flows," NASA, NASA Ames Research Center Moffet Field, Santa Clara, CA, Report No. 19930013620.
[37] Thollet, W., 2017, "Body Force Modeling of Fan-Airframe Interactions," Ph.D. thesis, Université de Tolouse – ISAE, Toulouse, France.
[38] Magrini, A., 2022, "Body Force Model Implementation of Transonic Rotor for Fan/Airframe Simulations," Aerospace, **9**(11), p. 725.
[39] Hughes, C. E., Jeracki, R. J., Woodward, R. P., and Miller, C. J., 2005, "Fan Noise Source Diagnostic Test - Rotor Alone Aerodynamic Performance Results," NASA Glenn Research Center, Cleveland, OH, Report No. TM-2005-211681.
[40] Van Zante, D. E., Podboy, G. G., Miller, C. J., and Thorp, S. A., 2009, "Testing and Performance Verifi Cation of a High Bypass Ratio Turbofan Rotor in an Internal Flow Component Test Facility," NASA Glenn Research Center, Cleveland, OH, Report No. TM-2009-215661.
[41] SAE, 1978, "Gas Turbine Engine Inlet Flow Distortion Guidelines," SAE Paper No. ARP1420.
[42] SAE, 1994, "Inlet Total-Pressure-Distortion Considerations for Gas-Turbine Engines," SAE Paper No. AIR1419C.
[43] Balandat, M., Karrer, B., Jiang, D. R., Daulton, S., Letham, B., Wilson, A. G., and Bakshy, E., 2019, "BoTorch: Programmable Bayesian Optimization in PyTorch," CoRR.
[44] Bevington, P. R., and Robinson, K. D., 2002, *Data Reduction and Error Analysis for the Physical Sciences/Philip R. Bevington*, McGraw-Hill, New York.
[45] Ding, C., and Peng, H., 2003, "Minimum Redundancy Feature Selection From Microarray Gene Expression Data," Computational Systems Bioinformatics. Proceedings of the 2003 IEEE Bioinformatics Conference. CSB2003, Stanford, CA, Aug. 11–14, pp. 523–528.